

Classic analogue of Autler-Townes-splitting transparency using a single magneto-optical ring resonator

Liting Wu(吴利婷), Wenkang Cao(曹文康), and Haolin Jiang(蒋昊林)
Citation: Chin. Phys. B, 2023, 32 (**10**): 104201. DOI: 10.1088/1674-1056/acd9c1
Journal homepage: http://cpb.iphy.ac.cn; http://iopscience.iop.org/cpb

What follows is a list of articles you may be interested in

Engineered photonic spin Hall effect of Gaussian beam in antisymmetric parity-time metamaterials

Lu-Yao Liu(刘露遥), Zhen-Xiao Feng(冯振校), Dong-Mei Deng(邓冬梅), and Guang-Hui Wang(王光辉)
Chin. Phys. B, 2023, 32 (**9**): 094201. DOI: 10.1088/1674-1056/accb89

Real-time and high-transmission middle-infrared optical imaging system based on a pixel-wise metasurface micro-polarization array

Lifeng Ma(马丽凤), Shan Du(杜杉), Jun Chang(常军), Weilin Chen(陈蔚霖), Chuhan Wu(武楚晗), Xinxin Shi(石鑫鑫), Yi Huang(黄翼), Yue Zhong(钟乐), and Quanquan Mu(穆全全)
Chin. Phys. B, 2023, 32 (**8**): 084201. DOI: 10.1088/1674-1056/acaa25

Research on the model of high robustness computational optical imaging system

Yun Su(苏云), Teli Xi(席特立), and Xiaopeng Shao(邵晓鹏)
Chin. Phys. B, 2023, 32 (**2**): 024202. DOI: 10.1088/1674-1056/ac9b34

Bandwidth expansion and pulse shape optimized for 10 PW laser design via spectral shaping

Da-Wei Li(李大为), Tao Wang(王韬), Xiao-Lei Yin(尹晓蕾), Li Wang(王利), Jia-Mei Li(李佳美),Hui Yu(余惠), Yong Cui(崔勇), Tian-Xiong Zhang(张天雄), Xing-Qiang Lu(卢兴强), and Guang Xu(徐光)
Chin. Phys. B, 2022, 31 (**9**): 094210. DOI: 10.1088/1674-1056/ac6018

Dynamically tunable multiband plasmon-induced transparency effect based on graphene nanoribbon waveguide coupled with rectangle cavities system

Zi-Hao Zhu(朱子豪), Bo-Yun Wang(王波云), Xiang Yan(闫香), Yang Liu(刘洋), Qing-Dong Zeng(曾庆栋), Tao Wang(王涛), and Hua-Qing Yu(余华清)
Chin. Phys. B, 2022, 31 (**8**): 084210. DOI: 10.1088/1674-1056/ac7e39

Classic analogue of Autler–Townes-splitting transparency using a single magneto-optical ring resonator

Liting Wu(吴利婷)[1,†], Wenkang Cao(曹文康)[2], and Haolin Jiang(蒋昊林)[3]

[1] *School of Information and Communication Engineering, Nanjing Institute of Technology, Nanjing* 211167, *China*
[2] *School of Mechanical Engineering, Guizhou University, Guiyang* 550025, *China*
[3] *School of Electronics and Information Engineering, Nanjing University of Information Science and Technology, Nanjing* 210044, *China*

(Received 26 February 2023; revised manuscript received 21 May 2023; accepted manuscript online 30 May 2023)

We show that an optical transparency can be obtained by using only one single magneto-optical ring resonator. This effect is based on the splitting of counterclockwise and clockwise modes in the ring resonator. Within a proposed resonator-waveguide configuration the superposition between the two degeneracy broken modes produces a transparency window, which can be closed, open, and modified by tuning the applied magnetic field. This phenomenon is an analogue of Autler–Townes splitting, and the magnetic field is equivalent to the strong external pump field. We provide a theoretic analysis on the induced transparency, and numerically demonstrate the effect using full-wave simulation. Feasible implication of this effect and its potential applications are also discussed.

Keywords: magneto-optic effect, dynamic tunable, single optical ring resonator

PACS: 42.15.Eq, 42.79.Ci, 78.20.Ls **DOI:** 10.1088/1674-1056/acd9c1

1. Introduction

The coherent interaction of photon with atoms have attracted much attention in the recent decades such as electromagnetically induced transparency (EIT)[1–5] and Autler–Townes splitting (ATS).[6–13] ATS is the splitting of energy levels induced by the strong field-driven interactions and quantified by a transparency window in the absorption or transmission spectrum.[6] Various application explorations have also been proposed in the decades, which include millimeter wave detection,[9] light storage,[10] optical isolation,[11] and transfer of orbital angular momentum.[12] Simultaneously, the concept of ATS has been transferred to other disciplines of physics, such as nano-structured metamaterials and coupled resonator arrays.[14–26] Especially, on-chip sensors or nanoparticle detection can be achieved by utilizing ATS-like effect.[16,17,22]

Both optical ring resonator (ORR)[27–30] and whispering-gallery micro-resonator (WGMR)[15–17,31,32] are the promising platforms for classic and all-optical analogs of ATS. Similar to ATS, at least two resonances with different frequencies should be properly designed and introduced so that light interacts with them simultaneously or in some order.[14–25] For example, Peng *et al.* provided an experimental observation of ATS-like spectra in integrated on-chip WGMR systems where the input wave interacts with the two coupled WGMRs.[20] In addition, an optical on-chip single microcavity system leading to ATS-like transparency is considered by introducing surface roughness,[14,18,19] material inhomogeneity,[26] or the presence of scatterers[16,17,22] in ORR or WGMR, and it has the obvious advantages of an easily fabrication and a compact size for better integration.

In this article, we propose a scheme in achieving an ATS-like transparency by using only one single homogeneous resonator without introducing any roughness or scatterers in an ORR. The key of this scheme is to utilize the splitting of counterclockwise and clockwise modes in a single magneto-optical (MO) ORR.[33] An ORR-waveguide configuration design is provided, which can simultaneously excite and utilize the counterclockwise and clockwise modes. When the mode degeneracy is broken, a transparency window is produced, which can be closed, open, and modified by tuning the applied magnetic field H_0. We argue that this effect is very similar to that of ATS in quantum optics, and the external magnetic field H_0 plays the role of strong pumping field that induces a level splitting in ATS.[6,20] Numerical full-wave simulation proves the feasibility of this scheme. Practical consideration on realization and implication of this scheme, e.g., by using available MO materials with a reduced geometric size, and the applicable frequency band of this scheme are discussed.

2. Theory and simulation

2.1. Proposal

Here we propose an induced transparency effect by using a single ORR. If we look at one ORR or equivalently a WGMR as shown in Fig. 1(a), we notice that it supports both clockwise and counter-clockwise modes simultaneously. The energy fluxes of them are opposite with each other, and can be characterized by the associated optical orbital angular momentum (OAM) of $\pm m$. We are interested in the frequency

[†]Corresponding author. E-mail: njltwu@hotmail.com

© 2023 Chinese Physical Society and IOP Publishing Ltd

regime about a single resonance, thus we would like to neglect the exact value of m for the sake of simplicity. We represent the clockwise mode with positive OAM by L in characterizing its left-handed nature, while the counter-clockwise with negative OAM by R. Albeit the L and R modes are degenerated in frequency if the ORR medium is isotropic, only one mode can be efficiently excited by an adjacent common waveguide bus.[28,30] For example, if a wave is incident from the upper common bus of Fig. 1(a) from the left side (represented by b_0), only the L mode is excited.

To excite both the L and R modes in a single ORR simultaneously, we propose a compact ORR-waveguide configuration as shown in Fig. 1(a). The incident wave is coupled into two identical common buses with field amplitudes $b_0 = a_0$. An ORR is placed between the two common buses. The field in the upper bus excites the L mode only, while that from the lower bus excites the R mode. The output field characterized by a complex transmission coefficient t is obtained by considering the superposition between the transmitted field components b_t and a_t [see Fig. 1(c)]. To mimic the split energy level in ATS, we utilize the MO effect[33–39] to lift the degeneracy of the L and R modes [see Fig. 1(b)]. A close analogue with the strong-coupling-field-induced energy level splitting in ATS is realized. The external applied magnetic field H_0 is equivalent to the strong pump beam in ATS, and its magnitude determines the splitting of the L and R modes.[33] The resonances of L and R modes induce strong dispersion on the corresponding guided field in each common bus, and produce a transparency window in the output spectrum t.

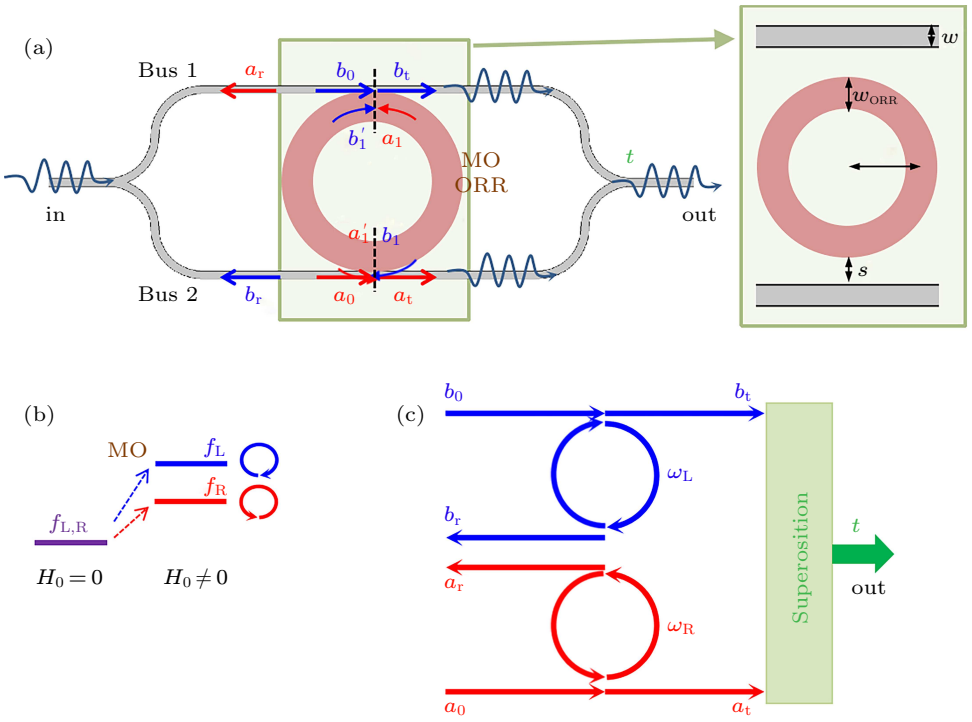


Fig. 1. (a) Schematic of the proposed ORR-waveguide structure. The input bus is split into two identical common buses with an MO ORR placed in between. Inset is the geometry parameters of the structure, which is marked in green in panel (a). (b) Magneto-optic effect is introduced into the ORR to break the degeneracy of the L and R modes. (c) Wave in the upper bus excites the L mode, while that in the lower bus excites the R mode. The output wave characterized by t exhibits the superposition between the degeneracy broken L and R modes.

2.2. Formulae

The influence of MO effect over L and R modes can be briefly understood by the treatment proposed in Ref. [33]. Under the excitation of an external magnetic field H_0, without loss of generality we can assume that the permittivity tensor of the MO ORR is expressed as

$$\overline{\varepsilon} = \begin{bmatrix} \varepsilon_r & j\varepsilon_k & 0 \\ -j\varepsilon_k & \varepsilon_r & 0 \\ 0 & 0 & \varepsilon_{\parallel} \end{bmatrix}, \tag{1}$$

where the z direction is taken to be normal to the 2D plane shown in Fig. 1(a). For the transverse magnetic (TM) polarized (i.e., magnetic filed along the z direction) mode, the corresponding effective refractive index is given by $n_{\text{eff}}^2 = (\varepsilon_r^2 - \varepsilon_k^2)/\varepsilon_r$. With increasing off-diagonal element ε_k the effective refractive index n_{eff} reduces, so the resonances of L and R modes blue shift. The off-diagonal element ε_k also determines the broken symmetry between L and R modes, and the splitting Δf is proportional to $\varepsilon_k/(\varepsilon_r^2 - \varepsilon_k^2)$.[33] If it is the permeability tensor $\overline{\mu}$ that becomes anisotropic in MO effect, similar effect can apply to the transverse electrical (TE) polarization.

To study the ATS-like transparency in the configuration

shown in Fig. 1(a), we neglect details on the level splitting of L and R modes, and assume that they are represented by effective indexes $n_{\rm L}$ and $n_{\rm R}$, respectively. By labeling the field components at each contact point as those shown in Fig. 1(a), and assuming that the self- and cross-coupling coefficients of L and R modes to the upper (lower) common bus are $\gamma_{\rm u}$ and $\kappa_{\rm u}$ ($\gamma_{\rm l}$ and $\kappa_{\rm l}$), respectively, we obtain a set of equations as follows:

$$a_1 = (\gamma_{\rm l} a_1' + \kappa_{\rm l} a_0) {\rm e}^{{\rm j}\phi_{\rm R}/2}, \tag{2}$$

$$a_1' = \gamma_{\rm u} a_1 {\rm e}^{{\rm j}\phi_{\rm R}/2}, \tag{3}$$

$$b_1 = (\gamma_{\rm u} b_1' + \kappa_{\rm u} b_0) {\rm e}^{{\rm j}\phi_{\rm L}/2}, \tag{4}$$

$$b_1' = \gamma_{\rm l} b_1 {\rm e}^{{\rm j}\phi_{\rm L}/2}, \tag{5}$$

where

$$\phi_{\rm L,R} = \pi n_{\rm L,R} d f/c, \tag{6}$$

d is the diameter of ORR, $f = \omega/2\pi$ is the frequency, $\gamma_{\rm u,l}$ are real, while $\kappa_{\rm u,l}$ are imaginary, with $\gamma_{\rm u,l}^2 - \kappa_{\rm u,l}^2 = 1$.

Solving the above equation set we can find that the field inside the ORR is enhanced by factors

$$q_{\rm R} = |\frac{a_1}{a_0}| = \frac{\kappa_{\rm l}}{|1 - \gamma_{\rm u}\gamma_{\rm l}{\rm e}^{{\rm j}\phi_{\rm R}}|}, \tag{7}$$

$$q_{\rm L} = |\frac{b_1}{b_0}| = \frac{\kappa_{\rm u}}{|1 - \gamma_{\rm u}\gamma_{\rm l}{\rm e}^{{\rm j}\phi_{\rm L}}|}. \tag{8}$$

The magnitudes of $q_{\rm L,R}$ are maximum at the Fabry–Pérot-like resonances $f_{\rm L,R}$ given by $\phi_{\rm L,R} = 2|m|\pi$, i.e.,

$$f_{\rm L,R} = 2|m|\frac{c}{d n_{\rm L,R}}, \tag{9}$$

where $\pm m$ is the topological indexes of the L and R modes.

The complex transmission coefficient t detected at the output port is given by

$$t = \frac{\gamma_{\rm l} a_0 + \kappa_{\rm l} a_1' + \gamma_{\rm u} b_0 + \kappa_{\rm u} b_1'}{a_0 + b_0}, \tag{10}$$

which, with $a_0 = b_0$, can be explicitly expressed as

$$t = \frac{1}{2}\Big(\frac{\gamma_{\rm l} - \gamma_{\rm u}{\rm e}^{{\rm j}\phi_{\rm R}}}{1 - \gamma_{\rm u}\gamma_{\rm l}{\rm e}^{{\rm j}\phi_{\rm R}}} + \frac{\gamma_{\rm u} - \gamma_{\rm l}{\rm e}^{{\rm j}\phi_{\rm L}}}{1 - \gamma_{\rm u}\gamma_{\rm l}{\rm e}^{{\rm j}\phi_{\rm L}}}\Big){\rm e}^{{\rm j}n_{\rm b}ks}, \tag{11}$$

where $k = 2\pi f/c$, $n_{\rm b}$ and s are the refractive index and the path length of the common bus, respectively. In the case of $n_{\rm R} = n_{\rm L} = n$ and $\gamma_{\rm l} = \gamma_{\rm u} = \gamma$, t becomes

$$t = \gamma\frac{1 - {\rm e}^{{\rm j}\phi}}{1 - \gamma^2{\rm e}^{{\rm j}\phi}}{\rm e}^{{\rm j}n_{\rm b}ks}. \tag{12}$$

In the above consideration we have assumed that the path lengthes through the two common buses are same ($s_{\rm a} = s_{\rm b} = s$). If the path lengthes are unequal ($s_{\rm a} \neq s_{\rm b}$), additional item is introduced, which can also be utilized, e.g., for filter application.

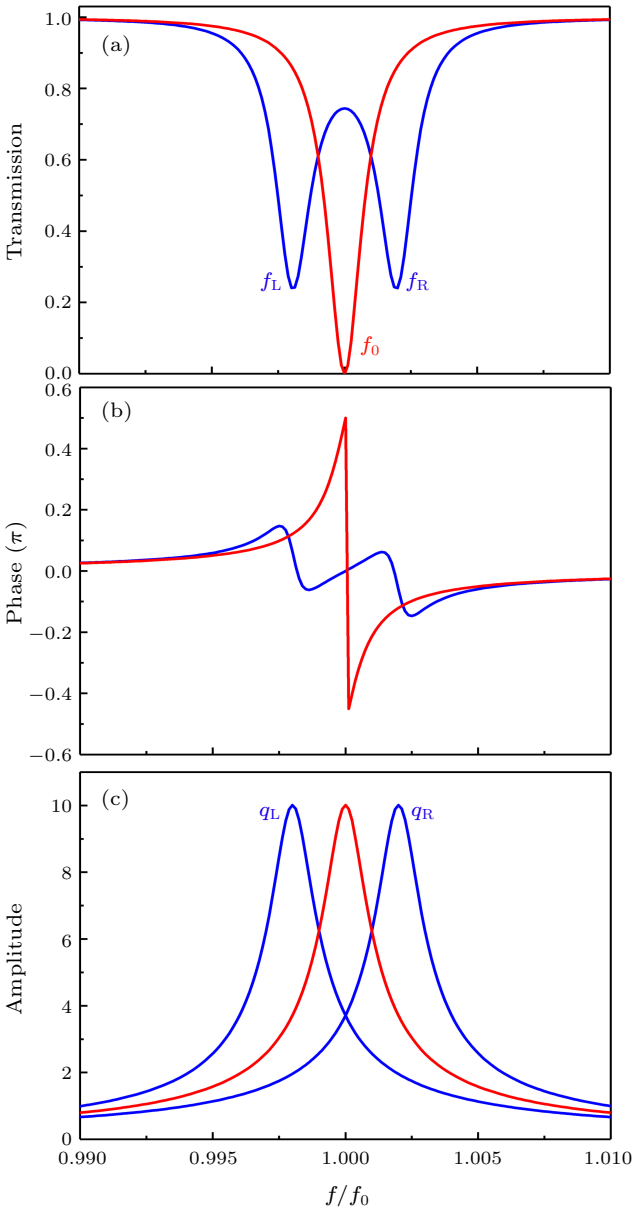


Fig. 2. Theoretical results on the (a) transmission spectra, (b) phase, and (c) $q_{\rm L}$ and $q_{\rm R}$ for symmetry conserved (red lines) and symmetry broken (blue lines) cases, respectively. Here $\gamma_{\rm l} = \gamma_{\rm u} = \gamma = 0.995$. In the symmetry conserved case, $f_{\rm L} = f_{\rm R} = f_0$. In the symmetry broken case, $f_{\rm L} = 0.998 f_0$ and $f_{\rm R} = 1.002 f_0$. The background phase term of $n_{\rm b}ks$ is neglected in panel (b).

Equation (11) depicts that the transmittance of this configuration is associated with the superposition between two Fabry–Pérot-like resonances of the L and R modes. Figure 2 shows an example on the transmission spectra and phase when the degeneracy of L and R modes is broken by the MO effect. We can see that, due to the mode splitting, the primary one resonance transmission dip splits into two separated ones about the L and R resonances. The initial smooth variation of phase from 0 to 2π is replaced by two Fano-like dispersions. We also calculate the field amplitude ratios of $q_{\rm L}$ and $q_{\rm R}$ characterizing the enhancement of field inside the MO ORR. As is expected, the ratios have their maximum values of $(1-\gamma^2)^{-0.5} \sim 10$ about the L and R resonances. Since the L and R modes have comparable quality-factors Q characterized

by Eqs. (7) and (8), and the above analysis does not involve the effective refractive of index that implies the interferences between two Fano resonances. This transparency is an ATS-like one.[16,22,25]

2.3. Simulation verification

In the above analysis we have neglected the possible dispersions over the refractive indexes (n, $n_{\rm L}$, and $n_{\rm R}$) and coupling coefficients ($\gamma_{\rm u,l}$ and $\kappa_{\rm u,l}$). Radiation loss is also ignored. Here we perform a serial of full-field optical simulations by using the finite element method (FEM) to verify the above theoretical analysis. In the numerical simulations, width of the waveguide in forming the ORR and the common buses is $w_{\rm ORR} = w = 0.4$ mm, radius of the ORR is $\rho = 10.2$ mm. The two identical common buses are long enough to avoid the coupling between ORR and the curved waveguiding structure at the input and output sides. Refractive index of the common bus is set to be 2, and the surrounding medium is vacuum. For the sake of simplicity, we assume that the values of elements in the permittivity tensor of the MO ORR are constant, with $\varepsilon_{\rm r} = 4$.

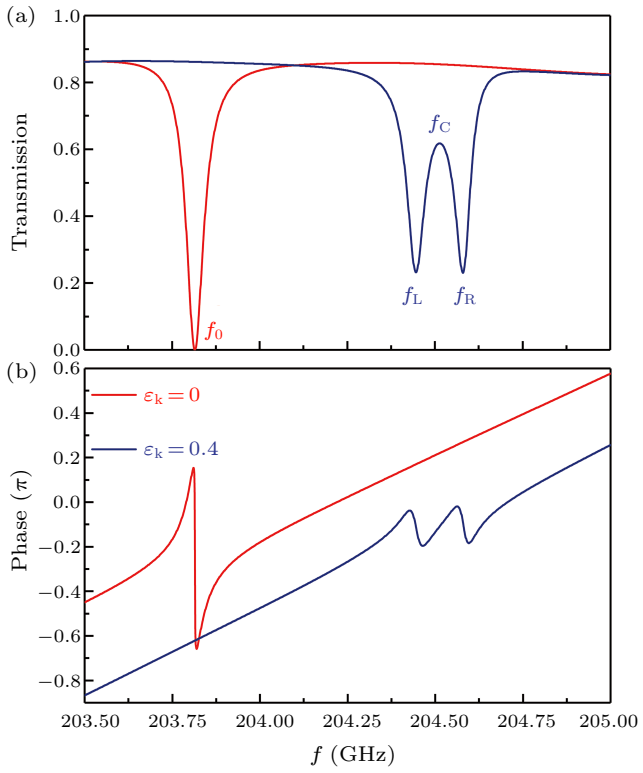


Fig. 3. Simulation results of (a) transmission spectra and (b) phase for $\varepsilon_{\rm k} = 0$ (red line) and $\varepsilon_{\rm k} = 0.4$ (blue line). Geometric parameters are $w_{\rm ORR} = w = 0.4$ mm, $\rho = 10.2$ mm, and $s = 0.6$ mm. The background contribution of $n_{\rm b}ks$ in Eqs. (11) and (12) is taken into account.

To emphasize the superposition described by Eq. (11) and get a clear exhibition on the associated field distributions, we firstly set the gap s between ORR and each bus to be 0.6 mm, and assume that the off-diagonal element $\varepsilon_{\rm k}$ is 0 and 0.4, respectively. The simulation results are shown in Figs. 3 and 4.

The maximum transmission coefficient $T = |t|^2$ does not reach 1 because the splitting and bending of the straight waveguide at the input and output ports in connection with the common buses produces a weak leakage damping on the guided modes.

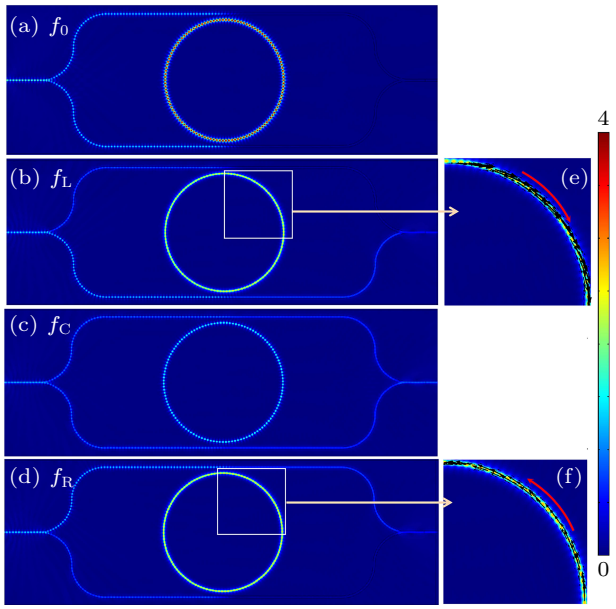


Fig. 4. Distribution of field amplitude H at (a) $f_0 = 203.815$ GHz, the transmission dip when $\varepsilon_{\rm k} = 0$, (b) $f_{\rm L} = 204.446$ GHz, (d) $f_{\rm R} = 204.58$ GHz, and (c) $f_c = 204.513$ GHz, when $\varepsilon_{\rm k} = 0.4$, respectively. (e) and (f) Zoomed-out images of the distribution of transverse energy flux inside the MO ORR. Geometric parameters are $w_{\rm ORR} = w = 0.4$ mm, $\rho = 10.2$ mm, and $s = 0.6$ mm.

From Figs. 3 and 4 we can see that when $\varepsilon_{\rm k} = 0$, where the resonances of L and R modes are degenerated ($f_{\rm L} = f_{\rm R} = f_0$), only one transmission dip at $f_0 = 203.815$ GHz can be observed. The phase of t possesses a single Fano-type shape. At the transmission dip f_0 the waves from the upper common bus and the lower one superpose with each other, especially inside the ORR [see Fig. 4(a)]. Transverse energy flux inside the ORR is zero due to the balanced contributions of L and R modes. The field components $b_{\rm t}$ and $a_{\rm t}$ are very weak.

When a nonzero $\varepsilon_{\rm k}$ of 0.4 is introduced, the transmission dip shifts to $f_{\rm C} = 204.513$ GHz. This blueshift can be explained because the corresponding effective refractive index is briefly given by $n_{\rm eff}^2 = (\varepsilon_{\rm r}^2 - \varepsilon_{\rm k}^2)/\varepsilon_{\rm r}$, which becomes smaller when $\varepsilon_{\rm k}$ increases. Furthermore, due to the MO effect the transmission dip splits into two separated ones, and produces a transparency window about $f_{\rm C}$. Phase of t is characterized by two correspondingly Fano-like shapes. For the distribution of field intensity, at the transmission dips of $f_{\rm L}$ and $f_{\rm R}$ shown in Figs. 4(b) and 4(d), field inside the MO ORR is almost homogenous because only one of the L and R modes dominates. The dominated mode determines the observable direction of transverse energy flux, see Figs. 4(e) and 4(f). Using Fig. 4(b) as an example here, at this frequency the L mode is resonant enhanced inside the MO ORR. As a result, the wave b_0 from the upper common bus is resonantly coupled into the MO ORR

via the Fabry–Pérot-like resonance of Eq. (8). This resonance substantially reduces the transmitted field b_t, and increases the reflected wave b_r. Superposition pattern between b_r and a_0 components can be clearly observed in the above section of the lower common bus. The field b_t in the later section of the upper common bus is zero. For the wave incident from the lower common bus, it is weakly coupled into the MO ORR because the R mode is out of resonance. For the induced transparency windows at f_C shown in Fig. 4(c), because the L and R modes are all out of resonance, the waves in both common buses do not efficiently coupled into the MO ORR, rending observable transmittance at the output port.

2.4. Further feasible analysis and discussion

With an academic curiosity, the FEM simulation presented in Subsection 2.3 demonstrates the physical mechanism of the proposed ATS-like transparency. A large ε_k value of 0.4 is considered. The geometric parameters are chosen in the way that the field is only moderated enhanced inside the MO ORR. However, in realistic situation a large ε_k value requires a huge external applied magnetic field H_0 that may beyond the-state-of-the-art techniques.[33,35,40] Also, it is interesting to ask whether the mechanism can be realized in structure with a compact size. A feasible analysis on these practical implication issues is required.

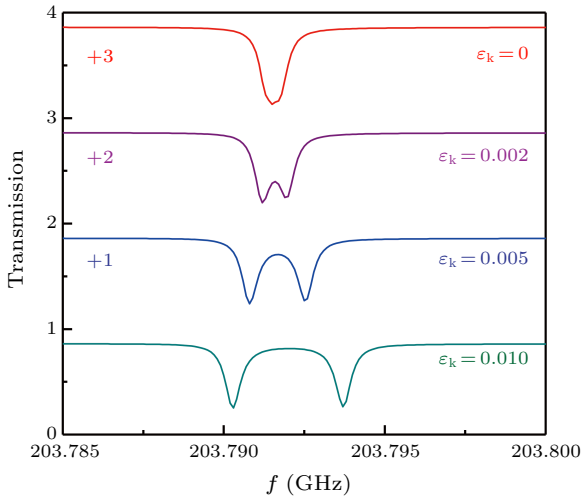


Fig. 5. Simulation results of the transmission spectra for different nonzero off-diagonal elements $\varepsilon_k = 0$, 0.002, 0.005, and 0.01, respectively. Here the distance s between the common bus and the MO ORR is increased to 1.15 mm to enhance the Q factor. Other parameters are $w_{ORR} = w = 0.4$ mm and $\rho = 10.2$ mm. In Bi:GdIG a field H_0 in the order of 0.02 T can easily render $\varepsilon_k = 0.002$.

For the first problem on the large value of ε_k, it can be easily avoided by increasing the $Q = f/\Delta f$ factor of the transmission dips. When the Q factor is increased, i.e., the dip width Δf is substantially reduced, it becomes easier to distinguish the weaker frequency split in L and R modes associated with a smaller ε_k value. An enhanced Q factor can be obtained by simply increasing the values of self-coupling coefficients γ_l and γ_u. Figure 5 shows the FEM simulation results when the distance between the common bus and the MO ORR is increased to 1.15 mm. We can see that the corresponding width Δf of the transmission dip becomes narrower, to ~ 0.001 GHz that is around two orders smaller than the value of 0.07 GHz shown in Fig. 3. Now we can distinguish the weak degeneracy broken modes and obtain a transparency window even at $\varepsilon_k = 0.002$. If Bi-doped gadolinium iron garnet $(GdBi)_3Fe_5O_{12}$ (Bi:GdIG) commercially available is utilized as the MO medium, a field H_0 in the order of 0.02 T[40] can easily excite the required nonreciprocal anisotropy.

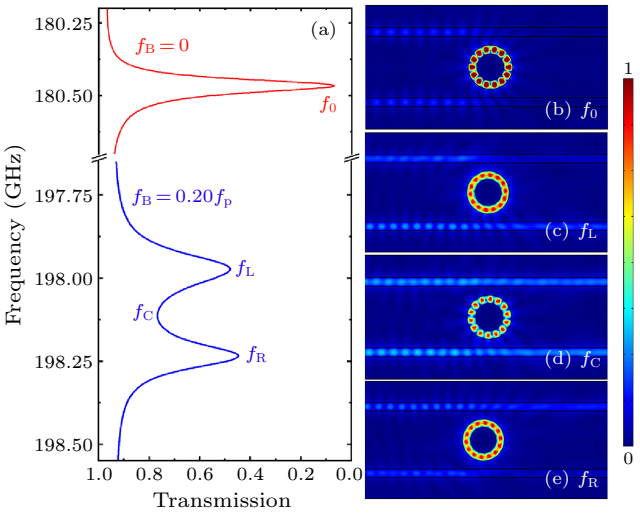


Fig. 6. Simulation results of (a) transmission spectra when $f_B = 0$ (red curve), and $0.20 f_p$ (blue curve), respectively. The distributions of field around the MO ORR at the transmission dips and transparency windows are plotted in (b) $f_0 = 180.466$ GHz, (c) $f_L = 197.971$ GHz, (d) $f_C = 198.111$ GHz, and (e) $f_R = 198.231$ GHz, respectively. Geometric parameters are $w_{ORR} = w = 0.4$ mm, $\rho = 0.8$ mm and $s = 0.38$ mm. The topological indexes of the L and R modes are $m = \pm 7$. This figure shows that the structure can be substantial reduced.

For the problem in applying this scheme to structure with a reduced geometric size, the main obstacle is the increased radiation loss and the corresponding reduced Q factor when the radius of the ORR decreases. We should utilize an MO material with a possible large ε_k value. Semiconductors with proper doping associated with strong dispersions on ε_r and ε_k can be utilized. Consider InSb with a doping density n of 3.747×10^{13} cm^{-3} as an example,[34] the elements of permittivity tensor are $\varepsilon_r = \varepsilon_\infty - f_p^2(f^2 - f_B^2 + jf^2\Gamma)^{-1}$, $\varepsilon_k = f_B f_p^2 f^{-1}(f^2 - f_B^2 + jf^2\Gamma)^{-1}$, and $\varepsilon_z = \varepsilon_\infty - f_p^2(f^2 + jf^2\Gamma)^{-1}$, respectively. Here $\varepsilon_\infty = 15.68$ is the permittivity at high frequency, $f_p = 464.45$ GHz is the bulk plasma frequency, and $\Gamma = 0.0001$ represents damping. A static magnetic field $H_0 = 0.05$ T can render $f_B = 0.20 f_p$. Figure 6 shows the FEM simulation results by using InSb in forming the MO ORR. Radius of the InSb ORR is 1 mm, and the gap between the ORR and each waveguide is 0.38 mm. All the other parameters are identical to these present before. We can see that an induced transparency can be obtained as well, and the topological index of the excited mode is reduced to C. Distributions of field

at the transmission dips and transparency window are similar to those in Fig. 4.

The exploration on this proposal is not limited to the above analysis. We also wander what is the applicable frequency range for this design and how to determine it. The frequency range of the ATS-like effect varies with different MO materials, which goes roughly from 5 GHz to 17 THz.[41–45] The effective frequency range for the given MO material is also worthy of study (see Appendix A). Meanwhile, it is interesting to study the influence of waveguide width in forming the MO ORR on the induced transparency window and the difference of ORR and cylinder (see Appendix B). Last but not least, can this proposal be verified by experiment and what are its applications? In fact, with the-state-of-the-art techniques researchers can fabricate ORRs for operation up to infrared and visible light already.[19,30,46,47] On-chip MO optical resonators monolithically integrated on silicon have also been demonstrated.[43,44] Particularly, Yuan *et al.* experimentally demonstrate an isolator with ultrahigh isolation ratios by coupling the MO material InSb with a ring resonator.[43] It further validates the experimental feasibility of our proposal. Since the values of ε_r and ε_k can be tuned by manipulating the external magnetic field H_0 [see Figs. 3 and 5], the proposed nonreciprocal induced transparency is dynamically tunable, to open, close, and change the transparency window for various applications that have been widely discussed in slow-light society.[48]

3. Conclusion

In summary, we have proved the feasibility in realizing an ATS-like transparency effect by using a single MO ORR. This effect is based on the mode splitting on the L and R modes in the MO ORR. Within a proposed ORR-waveguide configuration design the superposition between the two degeneracy broken modes produces a transparency window, which can be closed, open, and modified by tuning the external pump field (i.e. the applied magnetic field). We provide a theoretic analysis on the transmission, and numerically demonstrate the effect using FEM simulation. We also prove that the proposed scheme can be realized by MO materials commercially available. Such an analogue of ATS transparency and the associated slow light effect[48] can be subsequently utilized for various on-chip applications such as those in integrated optical circuits.[15,20]

Appendix A: Discussion of applicable frequency range

The above theoretical analyses and simulations show that the induced transparency window for the given OAM of $\pm m$ occurs in a narrowband. For example, in Subsection 2.3, the operating frequency is around 204 GHz when $|m| = 61$. From Eq. (9), we deduce that the two transmission dips can be tuned flexibly by changing the radius of MO ORR ρ or OAM of $\pm m$ for the given effective indexes $n_{L,R}$, which is related to ε_r and ε_k. However, in actual MO materials ε_r and ε_k are the functions of frequency, which limit greatly the frequency band of ATS-like effect. We take the MO material InSb with $f_B = 0.20 f_p$ discussed in Subsection 2.4 for illustration in the following.

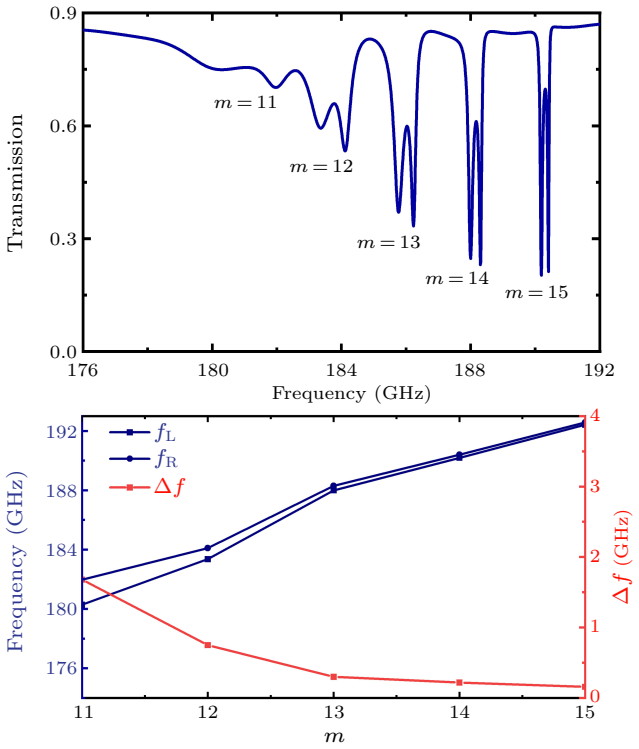


Fig. A1. (a) Simulation result of transmission spectra with different OAM of $\pm m$ when $f_B = 0.20 f_p$ and (b) the corresponding two transmission dips f_L, f_R and dip splitting Δf. Here the MO material is InSb with a doping density $n = 3.747 \times 10^{13}\text{cm}^{-3}$. Geometric parameters are $w_{ORR} = w = 0.4$ mm, $\rho = 2$ mm, and $s = 0.38$ mm. This figure shows the effective bandwidth of InSb under a static magnetic field H_0 of 0.05 T.

Figure A1(a) shows the FEM simulation result of transmission spectra at the frequency range from 176 GHz to 192 GHz, where the induced transparency windows with $|m| = 11, 12, 13, 14, 15$ are excited. Here the geometry parameters are $w_{ORR} = w = 0.4$ mm, $\rho = 2$ mm, and $s = 0.38$ mm. The frequency band is basically consistent with the theory. Due to $\varepsilon_r > \varepsilon_k > 0$, the operating frequency should satisfy $f > 173$ GHz. Then the splitting decreases with increasing frequency as shown in Fig. A1(b), which is in accordance with $\Delta f \propto \varepsilon_k/(\varepsilon_r^2 - \varepsilon_k^2)$.[33] For $|m| > 15$, it becomes more difficult to distinguish the weaker frequency splitting in L and R modes. In short, the effective range of f is about 176–192 GHz for InSb with the magnetic field $H_0 = 0.05$ T, and we can modify it by tuning the applied field for practical applications. For example, the applicable frequency range is about 170–190 GHz when $f_B = 0.18 f_p$, which can be easily achieved

by reducing H_0. Moreover, the applicable frequency range can be tuned by utilizing different MO materials.[41–45]

Appendix B: Influence of waveguide width in forming MO ORR

To better explore the influence of waveguide width $w_{\rm ORR}$ in forming MO ORR, we firstly set the permittivity tensors of the MO ORR and common bus are the same as those in Section 2.3, which ensures that $n_{\rm L}$ and $n_{\rm R}$ are constant and d is the only variable in Eq. (9). As shown in Fig. B1, L and R modes move to higher frequency and the frequency splitting increases with decreasing $w_{\rm ORR}$. Here other parameters are $w = 0.4$ mm, $s = 0.6$ mm, $\rho = 10.2$ mm, and $|m| = 61$. It can be explained by the equivalent diameter of MO ORR. Though ρ is a constant, the electromagnetic field in MO ORR is not uniformly distributed but concentrated on the outer side. That is to say, the decreasing $w_{\rm ORR}$ leads to the decreasing outer radius $\rho_{\rm out} = \rho + 0.5 w_{\rm ORR}$ and equivalent diameter of MO ORR d, in turn results in the increasing $f_{\rm L,R}$ and Δ_f.

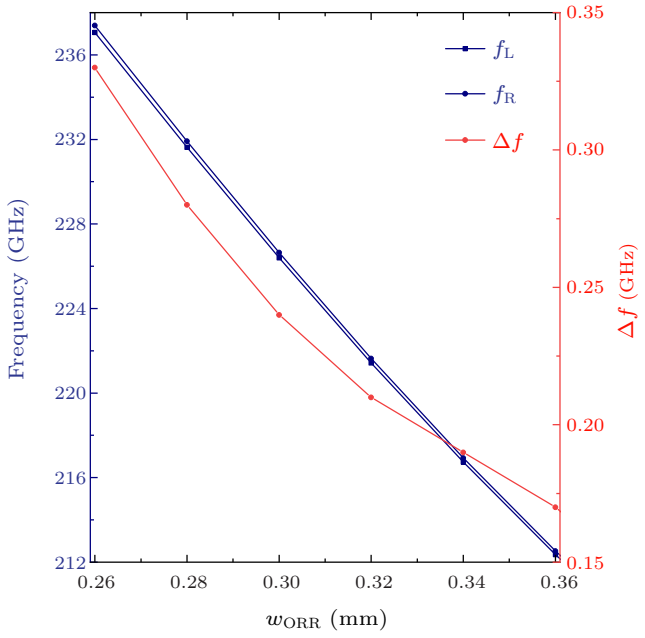


Fig. B1. The two transmission dips $f_{\rm L}$, $f_{\rm R}$ and dip splitting Δf versus width of the waveguide in forming MO ORR. Here the values of elements in the permittivity tensor of the MO ORR are constant, with $\varepsilon_{\rm r} = 4$ and $\varepsilon_{\rm k} = 0.4$. Other geometric parameters are $w = 0.4$ mm, $\rho = 10.2$ mm, and $s = 0.6$ mm. The topological indexes of the L and R modes are $m = \pm 61$.

Meanwhile, we prove the feasibility that the analogue of ATS transparency can be achieved when the MO ORR is replaced by an MO cylinder, which is just the limit case that $\rho_{\rm out} = w_{\rm ORR}$. To avoid the radiation loss when ρ is a small value, we take InSb with $f_{\rm B} = 0.20 f_{\rm p}$ for illustration. As shown in Fig. B2, $f_{\rm L,R}$ and Δ_f no longer change when $w_{\rm ORR}$ is greater than 0.7 mm. It is just the case that the equivalent diameter does not change when $w_{\rm ORR}$ is large enough. Here we set $\rho_{\rm out} = \rho + 0.5 w_{\rm ORR} = 1$ mm, $w = 0.4$ mm, and $s = 0.38$ mm. The FEM simulation results of field distribution in $f_{\rm L}$, $f_{\rm C}$, and $f_{\rm R}$ are shown in Figs. B3(b)–B3(d). Here $\rho_{\rm out} = w_{\rm ORR}$, i.e., the MO cylinder replaces the MO ORR. It is proved again that the outer radius of MO ORR $\rho_{\rm out}$ has greater influence on $f_{\rm L,R}$ and Δf.

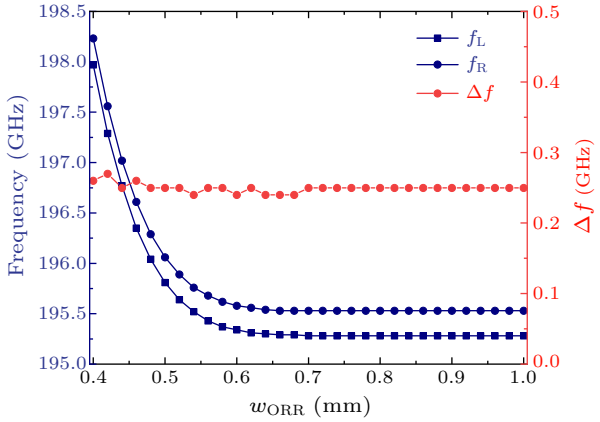


Fig. B2. The two transmission dips $f_{\rm L}$, $f_{\rm R}$ and dip splitting Δf versus width of the waveguide in forming MO ORR when $f_{\rm B} = 0.20 f_{\rm p}$. Other geometric parameters are $w = 0.4$ mm, $\rho_{\rm out} = \rho + 0.5 w_{\rm ORR} = 1$ mm, and $s = 0.38$ mm. Here the MO material is InSb with a doping density $n = 3.747 \times 10^{13}$ cm^{-13}. The topological indexes of the L and R modes are $m = \pm 7$.

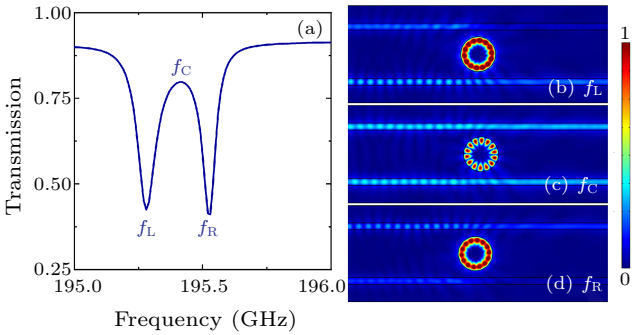


Fig. B3. Simulation results of (a) transmission spectra when $f_{\rm B} = 0.20 f_{\rm p}$. The distributions of field around the MO cylinder at the transmission dips and transparency window are plotted in (b) $f_{\rm L} = 195.286$ GHz, (c) $f_{\rm C} = 195.406$ GHz, and (d) $f_{\rm R} = 195.523$ GHz, respectively. Radius of the MO cylinder is 1 mm, other parameters are $w = 0.4$ mm and $s = 0.38$ mm. The topological indexes of the L and R modes are $m = \pm 7$.

Acknowledgments

This work was supported by the National Natural Science Foundation of China (Grant No. 12104227), the Scientific Research Foundation of Nanjing Institute of Technology (Grant No. YKJ202021), and the Guizhou Provincial Science and Technology Projects (Grant No. ZK [2022] general 035).

References

[1] Boller K J, Imamoğlu A and Harris S E 1991 *Phys. Rev. Lett.* **66** 2593
[2] Budker D, Kimball D, Rochester S and Yashchuk V 1999 *Phys. Rev. Lett.* **83** 1767
[3] Hau L V, Harris S E, Dutton Z and Behroozi C H 1999 *Nature* **397** 594
[4] Lukin M and Imamoğlu A 2001 *Nature* **413** 273
[5] Liu C, Dutton Z, Behroozi C H and Hau L V 2001 *Nature* **409** 490
[6] Autler S H and Townes C H 1955 *Phys. Rev.* **100** 703
[7] Sillanpää M A, Li J, Cicak K, Altomare F, Park J I, Simmonds R W, Paraoanu G S and Hakonen P J 2009 *Phys. Rev. Lett.* **103** 193601

[8] Zhang Y, Nie Z, Wang Z, Li C, Wen F and Xiao M 2010 *Opt. Lett.* **35** 3420
[9] Gordon J A, Holloway C L, Schwarzkopf A, Anderson D A, Miller S, Thaicharoen N and Raithel G 2014 *Appl. Phys. Lett.* **105** 024104
[10] Saglamyurek E, Hrushevskyi T, Rastogi A, Heshami K and LeBlanc L J 2018 *Nat. Photon.* **12** 774
[11] Sohn D B, örsel O E and Bahl G 2021 *Nat. Photon.* **15** 822
[12] Asadpour S H, Hamedi H R and Paspalakis E 2022 *Photonics* **9** 954
[13] Wu H, Ruan Y, Li Z, Dong M X, Cai M, Tang J, Tang L, Zhang H, Xiao M and Xia K 2022 *Laser Photon. Rev.* **16** 2100708
[14] Little B E, Laine J P and Chu S T 1997 *Opt. Lett.* **22** 4
[15] Naweed A, Farca G, Shopova S I and Rosenberger A 2005 *Phys. Rev. A* **71** 043804
[16] Zhu J, Özdemir S K, Xiao Y F, Li L, He L, Chen D R and Yang L 2010 *Nat. Photon.* **4** 46
[17] Zhu J, Özdemir S K, He L, Chen D R and Yang L 2011 *Opt. Express* **19** 16195
[18] Campanella C, Giorgini A, Avino S, Malara P, Zullo R, Gagliardi G and De Natale P 2013 *Opt. Express* **21** 29435
[19] Campanella C E, Mastronardi L, De Leonardis F, Malara P, Gagliardi G and Passaro V M 2014 *Opt. Express* **22** 25371
[20] Peng B, özdemir S K, Chen W, Nori F and Yang L 2014 *Nat. Commun.* **5** 5082
[21] Wei B and Jian S 2017 *J. Opt.* **19** 115001
[22] Zhi Y, Yu X C, Gong Q, Yang L and Xiao Y F 2017 *Adv. Mater.* **29** 1604920
[23] Yu L, Chen L, Zhang W, Zhang Y, Zhang Y, Kong L, Yan T and Li J 2019 *J. Lightwave Technol.* **37** 3620
[24] Ma K, Zhang Y, Su H, Yi G, Yu C and Wang J 2020 *Opt. Lett.* **45** 754
[25] Dyshlyuk A V, Eryusheva U A and Vitrik O B 2020 *J. Lightwave Technol.* **38** 6918
[26] Li W, Li J, Yu L, Feng Y, Yao Y, Sun Y, Zou Y and Xu X 2023 *APL Photon.* **8** 016102
[27] Yariv A, Xu Y, Lee R K and Scherer A 1999 *Opt. Lett.* **24** 711
[28] Heebner J E, Boyd R W and Park Q H 2002 *Phys. Rev. A* **65** 036619
[29] Heebner J E, Boyd R W and Park Q H 2002 *J. Opt. Soc. Am. B* **19** 722
[30] Poon J K, Scheuer J, Mookherjea S, Paloczi G T, Huang Y and Yariv A 2004 *Opt. Express* **12** 90
[31] Li B B, Xiao Y F, Zou C L, Liu Y C, Jiang X F, Chen Y L, Li Y and Gong Q 2011 *Appl. Phys. Lett.* **98** 021116
[32] Rosenberger A T 2013 *Adv. Slow Fast Light VI* **8636** 863602
[33] Wang J, Fung K H, Dong H Y and Fang N X 2011 *Phys. Rev. B* **84** 235122
[34] Yang M, Li T F, Sheng Q W, Guo T J, Guo Q H, Cui H X and Chen J 2013 *Opt. Express* **21** 25035
[35] Guo T J, Li T F, Yang M, Cui H X, Guo Q H, Cao X W and Chen J 2014 *Opt. Express* **22** 537
[36] Li Z, Wu R X, Li Q B and Poo Y 2015 *Appl. Opt.* **54** 1267
[37] Guo R P, Wu L T, Yang M, Guo T J, Cui H X, Cao X W and Chen J 2015 *Phys. Rev. A* **91** 023808
[38] Nezhad V F, You C and Veronis G 2021 *Chin. Opt. Lett.* **19** 083602
[39] Chen J, Pan J, Zheng Y, Liang W and Li Z Y 2022 *Chin. Opt. Lett.* **20** 053901
[40] Khurgin J B 2006 *Appl. Phys. Lett.* **89** 251115
[41] Wang Z, Chong Y, Joannopoulos J D and Soljačić M 2009 *Nature* **461** 772
[42] Mu Q, Fan F, Chen S, Xu S, Xiong C, Zhang X, Wang X and Chang S 2019 *Photon. Res.* **7** 325
[43] Bi L, Hu J, Jiang P, Kim D H, Dionne G F, Kimerling L C and Ross C 2011 *Nat. Photon.* **5** 758
[44] Yuan S, Chen L, Wang Z, Deng W, Hou Z, Zhang C, Yu Y, Wu X and Zhang X 2021 *Nat. Commun.* **12** 5570
[45] Shayegan K J, Zhao B, Kim Y, Fan S and Atwater H A 2022 *Sci. Adv.* **8** eabm4308
[46] Peng B, özdemir S K, Lei F, Monifi F, Gianfreda M, Long G L, Fan S, Nori F, Bender C M and Yang L 2014 *Nat. Phys.* **10** 394
[47] Chang L, Jiang X, Hua S, Yang C, Wen J, Jiang L, Li G, Wang G and Xiao M 2014 *Nat. Photon.* **8** 524
[48] Khurgin J B 2010 *Adv. Opt. Photon.* **2** 287